

OGLE-2015-BLG-0051/KMT-2015-BLG-0048Lb: A GIANT PLANET ORBITING A LOW-MASS BULGE STAR
DISCOVERED BY HIGH-CADENCE MICROLENSING SURVEYS

C. HAN¹, A. UDALSKI^{2,9}, A. GOULD^{3,4,10}, V. BOZZA^{5,6},

AND

Y. K. JUNG^{1,9}, M. D. ALBROW⁷, S.-L. KIM⁴, C.-U. LEE⁴, S.-M. CHA^{4,8}, D.-J. KIM⁴, Y. LEE^{4,8}, B.-G. PARK⁴, I.-G. SHIN^{1,9}
(THE KMTNET COLLABORATION),

M. K. SZYMAŃSKI², I. SOSZYŃSKI², J. SKOWRON², P. MRÓZ², R. POLESKI^{2,3}, P. PIETRUKOWICZ², S. KOZŁOWSKI², K. ULACZYK²,
Ł. WYRZYKOWSKI², M. PAWLAK²
(THE OGLE COLLABORATION),

¹ Department of Physics, Chungbuk National University, Cheongju 361-763, Republic of Korea

² Warsaw University Observatory, Al. Ujazdowskie 4, 00-478 Warszawa, Poland

³ Department of Astronomy, Ohio State University, 140 W. 18th Ave., Columbus, OH 43210, USA

⁴ Korea Astronomy and Space Science Institute, Daejeon 305-348, Republic of Korea

⁵ Dipartimento di Fisica "E. R. Caianiello", Università di Salerno, Via Giovanni Paolo II, 84084 Fisciano (SA), Italy

⁶ Istituto Nazionale di Fisica Nucleare, Sezione di Napoli, Via Cintia, 80126 Napoli, Italy

⁷ University of Canterbury, Department of Physics and Astronomy, Private Bag 4800, Christchurch 8020, New Zealand

⁸ School of Space Research, Kyung Hee University, Yongin 446-701, Republic of Korea and

⁹ Harvard-Smithsonian Center for Astrophysics, 60 Garden St., Cambridge, MA, 02138, USA

Draft version July 12, 2021

ABSTRACT

We report the discovery of an extrasolar planet detected from the combined data of a microlensing event OGLE-2015-BLG-0051/KMT-2015-BLG-0048 acquired by two microlensing surveys. Despite that the short planetary signal occurred in the very early Bulge season during which the lensing event could be seen for just about an hour, the signal was continuously and densely covered. From the Bayesian analysis using models of the mass function, matter and velocity distributions combined with the information of the angular Einstein radius, it is found that the host of the planet is located in the Galactic bulge. The planet has a mass $0.72^{+0.65}_{-0.07} M_J$ and it is orbiting a low-mass M-dwarf host with a projected separation $d_{\perp} = 0.73 \pm 0.08$ AU. The discovery of the planet demonstrates the capability of the current high-cadence microlensing surveys in detecting and characterizing planets.

Subject headings: gravitational lensing: micro – planetary systems

1. INTRODUCTION

Since the first discovery by Wolszczan & Frail (1992) followed by Mayor & Queloz (1995), many exo-planets have been discovered. With the *Kepler* mission, the number of known planets explosively increased and now exceeds ~ 3000 according to the Extrasolar Planets Encyclopaedia³. Most of them were discovered by either the transit, e.g. Tenenbaum et al. (2014), or radial-velocity methods, e.g. Pepe et al. (2011).

Planets have also been discovered using the microlensing method. Due to the fact that these planetary systems are detected through their gravitational fields rather than their radiation, this method makes it possible to detect planets around faint stars and even dark objects. Furthermore, microlensing is sensitive to planets in wide orbits beyond the snow line, which separates regions of rocky planet formation from regions of icy planet formation, while other major planet detection techniques are sensitive to close-in planets. Being able to detect planets that are difficult to be detected by other techniques, the method is important for the comprehensive understanding of planet formation (Gaudi 2012).

The number of known microlensing planets at the time of writing this paper is 46, which is relatively small compared to the number of planets detected by other major methods. There

are two main reasons for the small number of microlensing planets. The first reason is the rarity of microlensing events. The optical depth to microlensing, which represents the average probability of a star to be gravitationally lensed at a given moment, toward the Galactic bulge field is of order 10^{-6} (Sumi et al. 2003, 2006). Then, observation cadences of survey experiments were limited because they should monitor a large area of sky in order to maximize the number of observing stars. The second reason is the short duration of planetary microlensing signals. A planetary companion to a stellar lens exhibits its presence through a short-term perturbation to the smooth and symmetric lensing light curve induced by the host star (Mao & Paczynski 1991; Gould & Loeb 1992). It was difficult to cover such short planetary signals by early-generation lensing surveys that had $\sim 1/2 - 1$ day observation cadences. To detect short planetary signals, earlier lensing experiments adopted a strategy where lensing events were detected by wide-field surveys and events detected by surveys were intensively monitored using multiple narrow-field telescopes (Albrow et al. 1998). However, only a small fraction of ongoing events, which exceeds several hundreds during an observing season, could be observed by approximately a dozen follow-up telescopes. As a result, the detection efficiency of microlensing planets under the survey/follow-up mode observation had been low.

However, past few years have witnessed great changes in microlensing surveys. With the start of the fourth phase

⁹ The OGLE Collaboration

¹⁰ The KMTNet Collaboration

³ <http://exoplanet.edu>

survey experiment, the Optical Gravitational Lensing Experiment (OGLE: Udalski et al. 2015) group significantly increased the observation cadence by broadening the field of view of their camera from 0.4 deg^2 into 1.4 deg^2 . The Microlensing Observation in Astrophysics (MOA: Bond et al. 2001) group also plans to upgrade their camera to widen the current 2.2 deg^2 field of view into 4 deg^2 (T. Sumi, private communication). There were additions of instruments to microlensing surveys. The Wise team (Shvartzvald et al. 2014) joined microlensing surveys in 2011 by using its 1.0m telescope. The Korea Microlensing Telescope Network (KMT-Net) survey, that is composed of 3 globally distributed telescopes equipped with large-formation cameras, started microlensing observation in 2015 season. With the continuous and dense coverage of lensing events achieved by the instrumental upgrade of existing survey groups and the addition of new surveys, microlensing planet search is entering a new phase where planets can be detected by survey-mode observations alone.

In this paper, we report the discovery of a giant planet from the joint data acquired by the OGLE and KMTNet survey experiments. The short-lived planetary signal occurred in the very early Bulge season during which the event could be seen for just about an hour. Nevertheless, the signal was densely and continuously covered by the 2 surveys experiments, enabling to detect and characterize the planetary system.

The paper is organized as follows. In Section 2, we describe the observation of the planetary microlensing event by survey experiments and acquired data. In Section 3, we give a description about the modeling procedure conducted to analyze the observed lensing light curve. We provide the estimated physical parameters of the discovered planetary system in Section 4. Finally, we summarize results and make a brief discussion about the result in Section 5.

2. OBSERVATION AND DATA

The planet was discovered from the observation of a microlensing event OGLE-2015-BLG-0051 that occurred on a star located toward the Galactic bulge field. The equatorial coordinates of the lensed star (source) are (RA,DEC) = ($17^{\text{h}}58^{\text{m}}39^{\text{s}}.01, -28^{\circ}01'54''.1$), that correspond to the Galactic coordinates (l, b) = ($2.24^{\circ}, -2.00^{\circ}$).

The event was discovered by the OGLE Early Warning System (EWS: Udalski et al. 2015) on February 13, 2015 from observations using the 1.3m Warsaw telescope at the Las Campanas Observatory in Chile. On March 2, 2015, it was noticed that the event experienced an anomaly and an alert was issued to the microlensing community for follow-up observations. However, the alert was issued when the anomaly was almost finished and thus the major part of the anomaly could not be covered by follow-up observations.

The event was analyzed in real time with its progress. From the modeling conducted by one of us (CH) during the anomaly, it was pointed out that the anomaly was possibly of planetary origin, although other binary interpretations could not be completely excluded. Continued modeling conducted after the anomaly by CH and other modelers (VB and MDA) reached a consistent result that the anomaly was produced by a planetary companion to the lens.

Although the event could not be observed by follow-up observations, it was densely observed by the KMTNet lensing survey that is designed to monitor a large area of the Galactic bulge field with high cadences by using large-format cameras equipped on multiple telescopes. The KMTNet survey

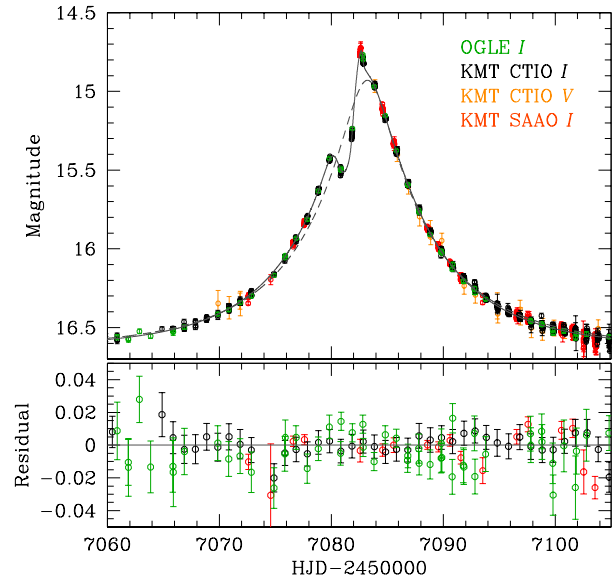


FIG. 1.— Light curve of the microlensing event OGLE-2015-BLG-0051/KMT-2015-BLG-0048. The solid curve superposed on the data is the model light curve based on the planetary model, while the dashed curve is based on the point-source point-lens (PSPL) model. Residuals of the KMT data sets are daily binned.

started its test observation in February, 2015, which matches the occurrence time of the event. The event was dubbed as KMT-2015-BLG-0048 in the KMT event list.⁴ The survey uses three identical telescopes that are located at Cerro Tololo Interamerican Observatory in Chile (KMT CTIO), South African Astronomical Observatory in South Africa (KMT SAAO), and Siding Spring Observatory in Australia (KMT SSO). At the time of the event, KMT SSO was not online and the event was observed by two telescopes, KMT CTIO and KMT SAAO. Each telescope has a 1.6m aperture and is equipped with a mosaic camera composed of four $9\text{K} \times 9\text{K}$ CCDs. Each CCD has a pixel size of 10 microns corresponding to 0.4 arcsec/pixel and thus the camera has a 4 deg^2 field of view (Kim et al. 2016). For the major fields, the observation cadence of the survey is $\sim 10 \text{ min}$. This cadence is high enough to detect signals produced by Earth-mass planets considering that the perturbation time of the signal is $\sim 3 \text{ hr}$.

In our analysis, we use combined data acquired by the OGLE and KMTNet surveys. The OGLE data are composed of 1167 *I*-band images. The KMTNet data consist of 786 *I*-band and 54 *V*-band images obtained from KMT CTIO observations and 1117 *I*-band images acquired from KMT SAAO observations. The main use of the KMT CTIO *V*-band data is to constrain the source star but they are not used for the light curve analysis because (1) the number of data is small and (2) the photometry is relatively poor due to extinction. There exist data taken by the MOA group but we do not use them in our analysis not only because the perturbation region covered by the data overlaps with that covered by the combined OGLE+KMTNet data but also because the photometry quality is relatively poor.

Photometry of the images are conducted using the customized pipelines of the individual groups. Both pipelines are based on the Difference Imaging Analysis method

⁴ <http://astroph.chungbuk.ac.kr/~kmtnet>

TABLE 1
ERROR-BAR NORMALIZATION
PARAMETERS

| Data set | k | σ_{\min} (mag) |
|----------|-------|-----------------------|
| OGLE | 1.749 | 0.001 |
| KMT CTIO | 1.386 | 0.005 |
| KMT SAAO | 1.162 | 0.002 |

(Alard & Lupton 1998; Woźniak 2000; Albrow et al. 2009). Since data are taken by different telescopes and processed by different photometry codes, we renormalize error bars of the individual data sets by

$$\sigma' = k(\sigma_0^2 + \sigma_{\min}^2)^{1/2}, \quad (1)$$

where σ_0 is the error estimated from the pipeline, σ_{\min} is a factor used to make the cumulative distribution function of χ^2 as a function of lensing magnification linear, and k is a scaling factor to make χ^2 per degree of freedom become unity. Photometric precision improves as the source star is magnified and the factor σ_{\min} is needed to make the scatter of data points be consistent with the error bars of the source brightness. The scaling factor k is needed to ensure that each data set is fairly weighted according to its error bars. We note that the error-bar normalization parameters vary as a lensing model varies. We iterate the normalization process and the final parameters are set when the model is stable. In Table 1, we present the estimated normalization parameters of the individual data sets. Although the event was observed in the early season, we find no systematic trend in the photometry caused by airmass trends.

In Figure 1, we present the light curve of OGLE-2015-BLG-0051/KMT-2015-BLG-0048. Compared to the continuous and symmetric light curve of a single-mass event, the light curve exhibits a short-term perturbation during $7080.0 \lesssim \text{HJD} - 2450000 \lesssim 7082.5$. The perturbation shows a feature that is composed of a depression centered at $\text{HJD} - 2450000 \sim 7081.5$ and brief bumps at both edges of the depression. Such dips, usually surrounded by two bumps, are a generic feature of lensing systems with small mass ratios $q \ll 1$ and normalized planet-star separations $s < 1$, i.e., planets inside the Einstein ring, which represents the source image caused by the exact alignment of the source, lens, and observer. When a source is lensed by the host of a planet, the host star's gravity generates two images, one inside and the other outside the Einstein ring. The former, being a saddle point on the time delay surface, is easily suppressed if the planet lies in or near the path, thereby causing relative demagnification, and hence a dip in the light curve (Gaudi 2012).

Besides the main feature of the anomaly, there appears to exist a weak anomaly at $\text{HJD} \sim 2457075$, where 4 data points show a ~ 0.02 mag level deviation. We consider it as a fluctuation in data because (1) the deviation is consistent with 3σ level of photometry, (2) the region is sparsely observed, and (3) a 2-body model cannot explain both of this weak and the main anomaly features.

The major structure of the anomaly feature was well covered by the survey data despite the short time window toward the field. See the zoom of the light curve around the planetary perturbation presented in Figure 2. During the time of the perturbation when the Bulge field could be seen only for approximately an hour, the OGLE survey obtained 2 images per night and the KMTNet survey obtained up to 20 images

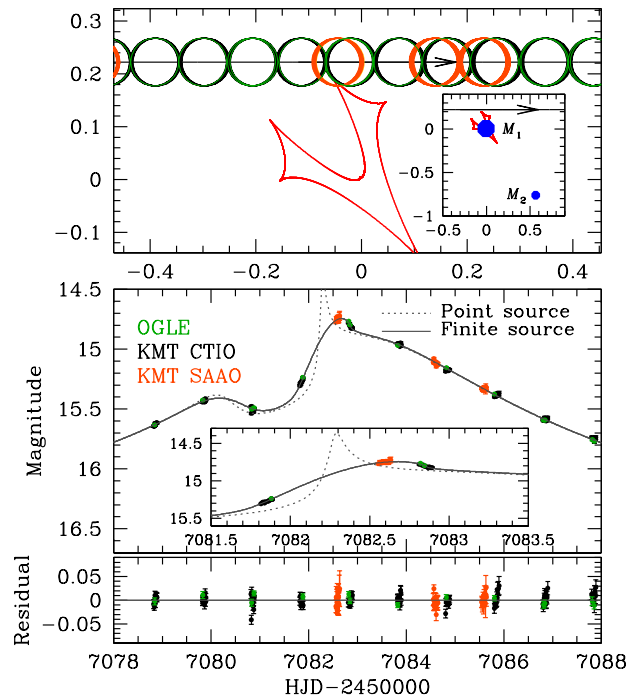


FIG. 2.— Lens system geometry. The upper panel shows the source trajectory (straight line with an arrow) with respect to the lens components (marked by M_1 and M_2) and caustics (closed concave curve) and the lower panel shows the light variation with the progress of the source position. Lengths are scaled to the Einstein radius and the source trajectory is aligned so that the progress of the source matches the light curve shown in the lower panel. The inset in the upper panel shows the wide view and the major panel shows the enlarged view around the caustic. The empty circles on the source trajectory represent the source positions at the times of observation and the size indicates the source size. The dotted curve in the lower panel is the light curve expected for a point source. The inset in the middle panel shows the zoom of the light curve affected by finite-source effects.

per night using its two telescopes. Since the OGLE and KMT CTIO telescopes are located at the sites with similar longitudes, the coverage of the perturbation by the two telescopes are similar. Although the KMT SAAO data missed the depression part of the perturbation due to poor weather conditions, they cover the second bump thanks to ~ 6.1 -hour longitude difference from the Chilean telescopes.

3. ANALYSIS

Keeping in mind that the anomaly pattern is likely to be produced by a binary lens with a low mass ratio, we conduct binary-lens modeling. For the description of a binary-lensing light curve, one needs 7 principal parameters for the lensing system and 2 flux parameters for each observatory. The first 3 of the principal parameters describe the source approach with respect to the lens, including the time of the closest source approach to a reference position of the lens, t_0 , the lens-source separation at that moment, u_0 (impact parameter), and the time for the source to cross the angular Einstein radius θ_E of the lens, t_E (Einstein time scale). For the reference position of the lens, we use the barycenter of the binary lens. The other 3 principal parameters describe the binary lens including the projected separation s and the mass ratio q between the binary components, and the angle between the source trajectory and the binary axis, α . We note that the impact parameter u_0 and the binary separation s are normalized to θ_E . The other parameter defined as the ratio of the angular source radius to the Einstein radius, $\rho = \theta_*/\theta_E$, is needed to describe light curve

TABLE 2
LENSING PARAMETERS

| Parameters | Values |
|----------------------|-------------------------|
| χ^2 | 3057.1 |
| t_0 (HJD) | 2457083.081 ± 0.003 |
| u_0 | 0.224 ± 0.002 |
| t_E (days) | 10.81 ± 0.07 |
| s | 0.963 ± 0.002 |
| q (10^{-3}) | 7.43 ± 0.13 |
| α (rad) | 5.358 ± 0.002 |
| ρ (10^{-3}) | 45.3 ± 0.6 |
| f_b/f_s | 0.01 ± 0.01 |

deviations affected by finite-source effects. For the graphical presentation of the binary lensing parameters, see Figure 6 of Jung et al. (2015). The flux parameters f_s and f_b represent the fluxes from the source and blend, respectively.

For some lensing events, observed data exhibit subtle residuals from the best-fit model based on the principal lensing parameters due to higher-order effects. The known causes of such deviations include the parallax effect (Gould 1992) and the lens orbital effect (Albrow et al. 2000; An et al. 2002; Jung et al. 2013). The parallax effect is caused by the positional change of the observer due to the orbital motion of the Earth around the Sun. On the other hand, the lens-orbital effect is caused by the positional change of the lens due to its orbital motion. Such effects are important for long time-scale events where the duration of the event comprises a significant fraction of the orbital period of either the Earth or the lens. For OGLE-2015-BLG-0051/KMT-2015-BLG-0048 with an Einstein time scale $t_E \sim 11$ days, we find that these higher-order effects are negligible.

We proceed light-curve modeling in several steps. In the first step, we conduct a preliminary grid search for solutions in the parameter space of (s, q, α) , for which lensing light curves vary sensitively to the change of the parameters. In this process, other parameters, for which light curve varies smoothly to the change of the parameters, are searched for by using a downhill approach. For the downhill χ^2 minimization, we use the Markov Chain Monte Carlo (MCMC) method. The ranges of the s and q parameters inspected by the grid search are $-1.0 < \log s \leq 1.0$ and $-4.0 < \log q \leq 1.0$, respectively, and they are divided into 70×70 grids. The range of the source trajectory angle is $0 < \alpha \leq 2\pi$ and it is divided into 15 grids. We note that α is allowed to vary from each starting point while s and q are fixed during the model search. In the second step, we investigate possible local solutions in the parameter space in order to check the existence of degenerate solutions where different combinations of the lensing parameters result in similar light curves. In this process, we refine local solutions by allowing all parameters, including the grid parameters s , q and α in the preliminary search, to vary. Finally, we search for the global solution by comparing χ^2 values of the identified local solutions.

Lensing magnifications are affected by finite-source effects when the source is located close to or over caustics, which represent the positions on the source plane where the lensing magnification of a point source becomes infinite. Caustics of binary lenses form a single or multiple closed curves where each curve is composed of concave curves that meet at cusps. For the computation of lensing magnifications affected by finite-source effects, we use the ray-shooting method. In this method, rays are uniformly shot from the lens plane, bent

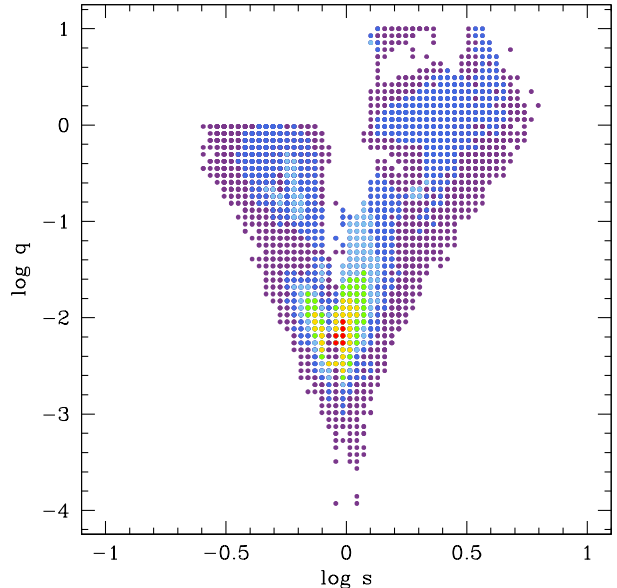


FIG. 3.— Map of $\Delta\chi^2$ in the (s, q) parameter space obtained from the preliminary grid search for lensing solutions. Color coding represents $n\sigma$ (red), $2n\sigma$ (yellow), $3n\sigma$ (green), $4n\sigma$ (cyan), $5n\sigma$ (blue), and $6n\sigma$ (purple), where $n = 20$. We note that the preliminary search is done before error-bar normalization and thus σ levels are different from the map presented in Fig. 4.

by the lens equation, and then collected on the source plane to make a ray map. The lens equation of a binary lens is expressed as

$$\zeta = z - \frac{\epsilon_1}{\bar{z} - \bar{z}_{L,1}} - \frac{\epsilon_2}{\bar{z} - \bar{z}_{L,2}}, \quad (2)$$

where ϵ_i is the mass fraction of each lens component, ζ , z , and $\bar{z}_{L,i}$ denote the positions of the source, image, and lens expressed in complex notation in units of the angular Einstein radius, respectively, and \bar{z} represents the complex conjugate of z (Witt 1990). Once a ray map is constructed, a finite-source magnification for a given source position is computed as the number density ratio of rays arrived on the source surface to the ray density on the image plane. In the initial grid search, we apply the map-making method (Dong et al. 2006), where a single map for a combination of the binary parameters s and q is used to produce many light curves resulting from different source trajectories. In the step to refine local solutions, the map-making method cannot be used because the parameters s and q are allowed to vary. In order to accelerate computation, we first apply semi-analytic hexadecapole approximations (Gould 2008; Pejcha & Heyrovský 2009) except when the source is on the caustic. We also minimize the number of rays by shooting rays that will arrive at regions around the caustic. Finally, we use customized codes developed for parallel computing, where multiple CPUs simultaneously compute model magnifications for the individual data points instead of computing the magnification of each data point one by one.

In computing finite-source magnifications, we consider the surface-brightness variation of the source star. For this, we model the surface-brightness profile as

$$S_\lambda \propto 1 - \Gamma_\lambda \left(1 - \frac{3}{2} \cos \phi \right), \quad (3)$$

where Γ_λ is the linear limb-darkening coefficient and ϕ is the angle between the line of sight toward the source and the nor-

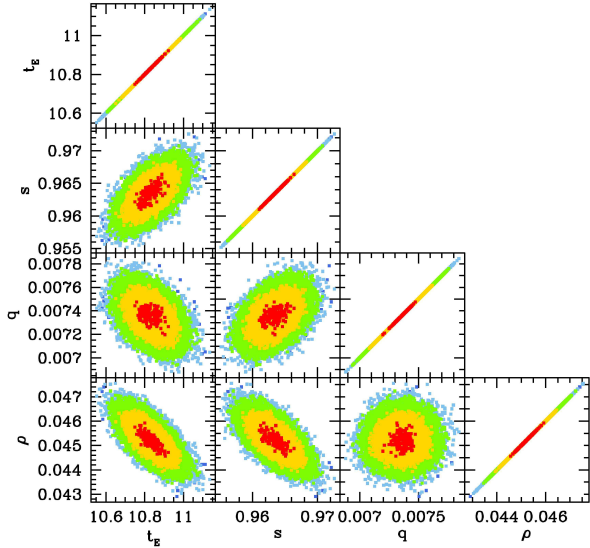


FIG. 4.— Distributions of the lensing parameters. The color coding represents points on the MCMC chains within 1σ (red), 2σ (yellow), 3σ (green), 4σ (cyan), and 5σ (blue) of the best-fit value.

mal to the source surface. We adopt $\Gamma_l = 0.46$ from Claret (2000) based on the de-reddened color and brightness of the source. See section 4 for details about the procedure to determine the color and magnitude.

From the search for a solution, we find a unique solution with a companion/primary mass ratio corresponding to a planetary case. We find no degenerate solution with a χ^2 value that is comparable to the best-fit solution. This can be seen in Figure 3, where we present the $\Delta\chi^2$ map in the (s, q) parameter space obtained from the preliminary grid search. By refining the solution, it is estimated that the planet/host mass ratio is $q = (6.80 \pm 0.18) \times 10^{-3}$ and the projected planet-host separation is $s = 0.954 \pm 0.004$. In Table 2, we present the best-fit lensing parameters. In Figure 4, we also present the distributions of the lensing parameters on the MCMC chain in order to show the covariances between the lensing parameters.⁵ The MCMC run is stopped by visually inspecting the posterior distributions in the parameter space. The uncertainty of each parameter is estimated from the scatter of the MCMC chain.

We note that the shape of the light curve resembles that of MOA-2007-BLG-192 (Bennett et al. 2008). For MOA-2007-BLG-192, the observational coverage of the planetary deviation is sparse and incomplete and thus there exist multiple possible solutions. On the other hand, the coverage of the deviation of OGLE-2015-BLG-0051 is dense and complete thanks to high-cadence observation from multiple distributed locations, leading to unambiguous characterization of the planetary system.

In the upper panel of Figure 2, we present the geometry of the lens system corresponding to the best-fit solution. Due to the resonance of the projected separation to θ_E , i.e. $s \sim 1$, the lens system forms a single caustic around the host of the planet. The source passed the backside of the arrowhead-shaped caustic. The depression in the light curve occurred

⁵ Those who want to reanalyze the event can download the MCMC chain and the light curve data at <http://astroph.chungbuk.ac.kr/~cheongho/OB150051/>.

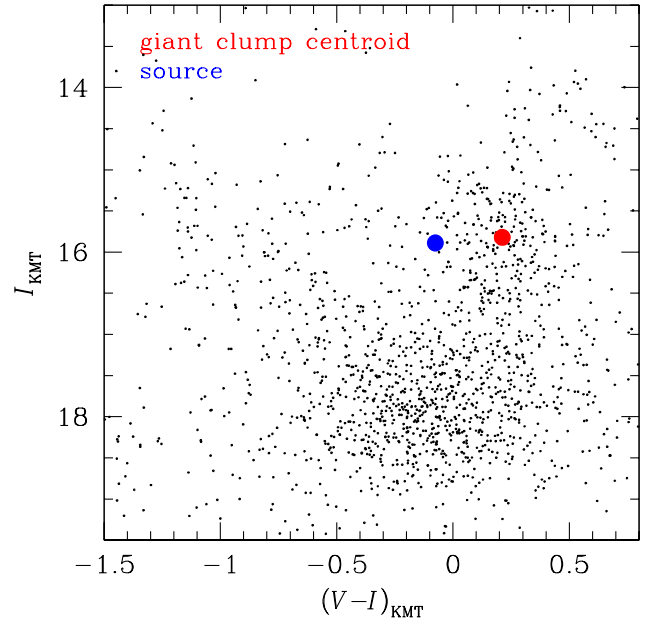


FIG. 5.— Source position in the instrumental color-magnitude diagram of nearby stars with respect to the centroid of the giant clump. The diagram is constructed based on stars in the KMT subfield ($140'' \times 140''$ area) including the source star.

when the source was in the demagnification valley between the two protrudent cusps that caused the brief bumps on both sides of the depression. The source crossed the tip of one of the cusps during which the light curve shows a clear finite-source signature from which we accurately measure the normalized source radius ρ . Considering that normalized source radii for typical lensing events produced by low-mass stars located roughly halfway between the source and observer are $\rho \sim 10^{-3}$ for events occurred on main-sequence stars and $\sim 10^{-2}$ even for events involved with giant source stars, the measured value of $\rho = (45.2 \pm 0.8) \times 10^{-3}$ is unusually large. For a given size of a bulge star, this suggests that the Einstein radius is very small.

4. PHYSICAL PARAMETERS

Since finite-source effects are clearly detected, it is possible to determine the angular Einstein radius from the relation

$$\theta_E = \frac{\theta_*}{\rho}. \quad (4)$$

The normalized source radius ρ is measured from the analysis of the light curve around the planetary perturbation. The angular radius of the source star, θ_* , is estimated from the source type that is determined based on the de-reddened color $(V-I)_0$ and brightness I_0 .

In order to determine the calibrated color and brightness of the source star, we use the method of Yoo et al. (2004). Following the method, we first locate the source star in the instrumental (uncalibrated) color-magnitude diagram of neighboring stars in the same field. We then calibrate the color and brightness from the offsets between the positions of the source star and the centroid of the giant clump (GC), for which its de-reddened color $(V-I)_{0,GC}$ and brightness $I_{0,GC}$ are known (Nataf et al. 2013). By adopting $(V-I)_{0,GC} = 1.06$ (Bensby et al. 2011) and $I_{0,GC} = 14.4$ accounting for a variation with Galactic longitude (Nataf et al. 2013), we find that $(V-I, I)_0 = (0.77 \pm 0.05, 14.5 \pm 0.03)$. This indicates that the

TABLE 3
PHYSICAL LENS PARAMETERS

| Parameter | Value |
|-----------------------|----------------------------------|
| Mass of the host star | $0.10^{+0.09}_{-0.01} M_{\odot}$ |
| Mass of the planet | $0.72^{+0.65}_{-0.07} M_J$ |
| Distance | 8.2 ± 0.9 kpc |
| Projected separation | 0.73 ± 0.08 AU |

source is a G-type giant star. We then convert $V-I$ into $V-K$ using the color-color relation of Bessell & Brett (1988) and finally determine θ_* using the color-angular radius relation of Kervella et al. (2004). We find that the angular source radius is $\theta_* = 4.40 \pm 0.38 \mu\text{as}$. We note that the two principal sources of uncertainty in estimating θ_* are the uncertainty of the dereddened color, $\sigma(V-I)_0 \sim 0.05$ mag, and the mag uncertainty in the determined position of GC, ~ 0.1 mag. These two sources combined yield a $\sim 7\%$ uncertainty in the estimated θ_* . On the other hand, the uncertainty in the color-size relation is small compared to the principal sources of error (Gould 2014). The angular Einstein radius estimated from θ_* is then

$$\theta_E = 0.093 \pm 0.008 \text{ mas.} \quad (5)$$

Combined with the Einstein time scale measured from the light curve modeling, the relative lens-source proper motion is determined as

$$\mu = \frac{\theta_E}{t_E} = 3.15 \pm 0.28 \text{ mas yr}^{-1}. \quad (6)$$

As expected from the large ρ , the estimated Einstein radius is significantly smaller than ~ 0.5 mas for typical events produced by low-mass stars.

For the unique determination of the mass M and distance D_L to the lens, it is required to measure both the lens parallax π_E and the Einstein radius θ_E (Gould 1992) that are related to the physical parameters by

$$M = \frac{\theta_E}{\kappa \pi_E} \quad D_L = \frac{\text{AU}}{\pi_E \theta_E + \pi_S}, \quad (7)$$

where $\kappa = 4G/(c^2 \text{AU}) \simeq 8.1 \text{ mas}/M_{\odot}$ and $\pi_S = \text{AU}/D_S$ is the parallax of the source star located at a distance D_S . For OGLE-2015-BLG-0051/KMT-2015-BLG-0048, the lens parallax cannot be measured due to the short time scale of the event and thus the physical parameters cannot be uniquely determined.

Although unique determinations are difficult, one can statistically constrain the physical lens parameters based on the measured Einstein radius θ_E and the relative lens-source proper motion μ combined with a Galactic model. For this, we conduct a Bayesian analysis by using models of the mass function, matter and velocity distributions. The Galactic model is based on Han & Gould (1995). In this model, the matter distribution is based on a double-exponential disk and a triaxial bulge. The disk velocity distribution is assumed to be Gaussian about the rotation velocity and the bulge velocity distribution is a triaxial Gaussian with components deduced from the flattening via the tensor virial theorem. The mass function is based on the Gould (2000) model, that includes stars, brown dwarfs and stellar remnants of white dwarfs, neutron stars, and black holes. Based on the Galactic model, we produce a large number (6×10^6) of artificial Galactic microlensing events and compute the relative probability of the individual events. From the lensing parameter

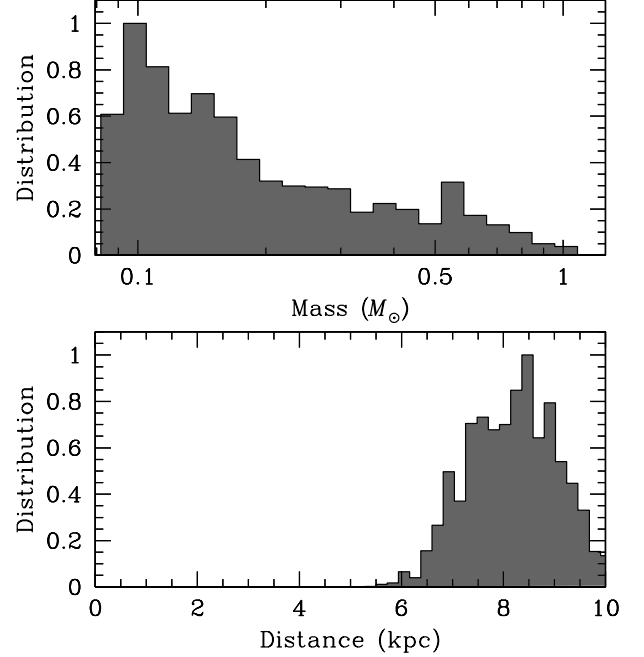


FIG. 6.— Posterior distributions of the lens mass and distance obtained from Bayesian analysis.

distribution of artificial events, we then estimate the range of the lens mass and distance corresponding to the measured t_E and θ_E .

Figure 6 shows the posterior distributions of the lens mass and distance obtained from Bayesian analysis. The mass and distance to the lens estimated by the Bayesian analysis are

$$M = 0.10^{+0.09}_{-0.01} M_{\odot}, \quad D_L = 8.2 \pm 0.9 \text{ kpc}, \quad (8)$$

respectively. We note that the upper and lower error bars of the mass are different due to the asymmetric distribution of the mass distribution. The estimated mass of the host corresponds to a low-mass star. However, considering that the likelihood of the lens mass peaks just above the lower limit of the assumed mass function, one cannot exclude the possibility that the host is a brown dwarf. We note that the mean value of the estimated distance to the lens approximately coincides with the adopted distance to the Galactic center $d_{GC} \sim 8$ kpc, implying that the source star is likely to be located behind the Galactic center and the lens is close to the Galactic center. This result comes from the fact that (1) the bulge self-lensing probability is higher for source stars behind the Galactic center due to the longer line of sight and (2) the lens density profile peaks at the Galactic center. We find that the blended light provides little constraint on the mass and distance distributions because the flux from the host star of the planet is negligible compared to the flux from the source star.

The measurement of q from the lens model then directly yields an estimate of the planet mass

$$M_p = qM = 0.72^{+0.65}_{-0.07} M_J, \quad (9)$$

while the measurement of s yields the projected lens-host separation

$$d_{\perp} = sD_L \theta_E = 0.73 \pm 0.08 \text{ AU}. \quad (10)$$

The snow line distance of the host star is $a_{sl} \sim 0.5$ AU according to the relation $a_{sl} = 2.7 \text{ AU}(M/M_{\odot})$ (Kennedy & Kenyon

2008). Therefore, the planet is located beyond the snow line of the host star.

5. SUMMARY AND DISCUSSION

We reported the discovery of an extrasolar planet that was detected from the combined data of a microlensing event OGLE-2015-BLG-0051/KMT-2015-BLG-0048 acquired by the OGLE and KMTNet surveys. Continuous and dense coverage of the short planetary signal by the survey data collected despite the short time window in the early bulge season enabled unambiguous detection and characterization of the planetary system. We find that the planet has a mass about twice that of the Jupiter and it is orbiting a low-mass host star located in the Galactic bulge. The discovery of the planet well demonstrates the capability of the current lensing surveys with enhanced observation cadence achieved by the instrumental upgrade of existing surveys and the addition of new surveys.

Cool M dwarfs far outnumber sun-like stars and thus understanding the process of planet formation around them is important. Furthermore, small masses and low luminosities

of M dwarfs provide leverage on conditions of planet formation, enabling to check the validity of existing formation theories and refine survived theories, e.g. (Ida & Lin 2005; Boss 2006). With improved survey capability, future microlensing planet sample will include planets not only in greatly increased number but also in wide spectrum of hosts and planets, helping us to have better and comprehensive understanding about the formation and evolution of planets.

Work by C. Han was supported by Creative Research Initiative Program (2009-0081561) of National Research Foundation of Korea. OGLE Team thanks Profs. M. Kubiak and G. Pietrzyński, former members of the OGLE team, for their contribution to the collection of the OGLE photometric data over the past years. The OGLE project has received funding from the National Science Centre, Poland, grant MAESTRO 2014/14/A/ST9/00121 to AU. Work by AG was supported by JPL grant 1500811. We acknowledge the high-speed internet service (KREONET) provided by Korea Institute of Science and Technology Information (KISTI). The KMTNet telescopes are operated by the Korea Astronomy and Space Science Institute (KASI).

REFERENCES

- Alard, C., & Lupton, Robert H. 1998, *ApJ*, 503, 325
 Albrow, M., Beaulieu, J.-P., Birch, P., et al. 1998, *ApJ*, 509, 687
 Albrow, M. D., Beaulieu, J.-P., Caldwell, J. A. R., et al. 2000, *ApJ*, 534, 894
 Albrow, M. D., Horne, K., Bramich, D. M., et al. 2009, *MNRAS*, 397, 2099
 An, J. H., Albrow, M. D., Beaulieu, J.-P., et al. 2002, *ApJ*, 572, 521
 Bensby, T., Adén, D., Meléndez, J., et al. 2011, *A&A*, 533, A134
 Bennett, D. P., Bond, I. A., Udalski, A., et al. 2008, *ApJ*, 684, 663
 Bessell, M. S., & Brett, J. M. 1988, *PASP*, 100, 1134
 Bond, I. A., Abe, F., Dodd, R. J., et al. 2001, *MNRAS*, 327, 868
 Boss, A. P. 2006, *ApJ*, 643, 501
 Claret, A. 2000, *A&A*, 363, 1081
 Dong, Subo, DePoy, D. L., Gaudi, B. S., et al. 2006, *ApJ*, 642, 842
 Gaudi, B. S. 2012, *ARA&A*, 50, 411
 Gould, A. 1992, *ApJ*, 392, 442
 Gould, A. 2000, *ApJ*, 539, 928
 Gould, A. 2014, *JKAS*, 47, 153
 Gould, A., & Loeb, A. 1992, *ApJ*, 396, 104
 Gould, A. 2008, *ApJ*, 681, 1593
 Han, C., & Gould, A. 1995, *ApJ*, 447, 53
 Henderson, C. B., Gaudi, B. S., Han, C. 2014, *ApJ*, 794, 52
 Ida, S., & Lin, D. N. C. 2005, *ApJ*, 625, 1045
 Jung, Y. K., Han, C., Gould, A., & Maoz, D. 2013, *ApJ*, 768, L7J
 Jung, Y. K., Udalski, A., Sumi, T., et al. 2015, *ApJ*, 798, 123
 Kennedy, G. M., & Kenyon, S. J. 2008, *ApJ*, 673, 502
 Kervella, P., Bersier, D., Mourard, D., et al. 2004, *A&A*, 428, 587
 Kim, S.-L., Lee, C.-U., Park, B.-G., et al. 2015, *Journal of the Korean Astronomical Society*, 49, 37
 Mao, S., & Paczynski, B. 1991, *ApJ*, 374, L37
 Mayor, M., & Queloz, D. 1995, *Nature*, 378, 355
 Nataf, D. M., Gould, A., Fouqué, P., et al. 2013, *ApJ*, 769, 88
 Pejcha, O., & Heyrovský, D. 2009, *ApJ*, 690, 1772
 Pepe, F., Lovis, C., Ségransan, D., *A&A*, 534, A58
 Shvartzvald, Y., Maoz, D., Kaspi, S., et al. 2014, *MNRAS*, 439, 604
 Sumi, T., Abe, F., Bond, I. A. 2003, *ApJ*, 591, 204
 Sumi, T., Woźniak, P. R., Udalski, A., et al. 2006, *ApJ*, 636, 240
 Tenenbaum, P., Jenkins, J. M., Seader, S., et al. 2014, *ApJS*, 211, 6
 Udalski, A., Szymański, M. K., & Szymański, G. 2015, *Acta Astron.*, 65, 1
 Witt, H. J. 1990, *A&A*, 236, 311
 Wolszczan, A., & Frail, D. A. 1992, *Nature*, 355, 145
 Woźniak, P. R. 2000, *Acta Astron.*, 50, 42
 Yoo, J., DePoy, D. L., Gal-Yam, A., et al. 2004, *ApJ*, 603, 139